Prediction of C_6–C_{12} Interconversion Rates Using Novel Zeolite-specific Kinetic Monte Carlo Simulation Methods

Mykela DeLuca, David D. Hibbitts*

Department of Chemical Engineering, University of Florida, Gainesville, FL 32611

Abstract

This study introduces a novel kinetic Monte Carlo (KMC) simulation package which models H-ZSM-5 crystals across experimentally relevant time and length scales to understand the role of transport during arene interconversion reactions (~100 reactions). This small subset of the methanol-to-hydrocarbon (MTH) network was previously modeled using periodic, dispersion-corrected density functional theory (DFT) to determine activation barriers and reaction energies for these KMC methods. Transport of arene molecules through the straight and sinusoidal channels of MFI was modeled as site-hopping and the DFT-calculated barriers are incorporated into the KMC model to account for mass-transport limitations. Barriers of different arene molecules trend well with their effective radii, and species with a smaller effective radii diffusive more readily. A previously published maximum rate analysis of arene interconversion pathways—previously validated by experimental data—is compared to a diffusion-free KMC model to confirm the accuracy of this KMC package. The temperature and pressure dependencies of rates obtained from KMC agree well with those of maximum rate analysis on the diffusion-free model, demonstrating that KMC effectively predicts rates as well as maximum rate analysis methods commonly used in kinetic applications of DFT. Arene interconversion pathways were also analyzed on KMC models incorporating diffusion to and from interior crystal sites. These simulations suggest that large species, such as hexamethylbenzene, become trapped at 10–20% of sites, thus causing site deactivation by limiting diffusion through MFI channels and lowering overall rates of product formation. Benzene diffusion barriers are artificially varied from 20–200 kJ mol^{-1} and rates of benzene methylation decrease by 4-fold with diffusion barriers greater than 80 kJ mol^{-1}; this suggests that species with diffusion barriers greater than 80 kJ mol^{-1} (such as penta- and hexamethylbenzene) will likely become trapped at interior sites and ultimately cause catalyst deactivation. This study serves as a proof-of-concept for a novel KMC package that expedites kinetic analysis of complex reaction pathways and introduces mass-transport limitations which are not commonly accounted for in kinetic DFT studies. This KMC package can predict the behavior of diffusion-limited species, such as penta- and hexamethylbenzene, and the mechanisms by which they are formed and eventually lead to catalyst deactivation.

1. Introduction

Arene methylation reactions are ubiquitous in industrial systems; they occur during the production of toluene from benzene and methanol-to-hydrocarbon (MTH) reactions. Zeolite surfaces, alkenes, and arenes are methylated by two methylation agents: methanol (CH_3OH) and dimethyl ether (CH_3OCH_3). The methylation of alkenes and arenes can occur through two well-established pathways: a sequential mechanism, in which the methylation agent first reacts with the zeolite to form a surface methyl:

$$CH_3OR + Z–H \rightarrow Z–CH_3 \quad (1)$$

preceding the methylation of a guest species:

$$C_nH_{2n} + Z–CH_3 \rightarrow C_nH_{2n+1} + Z–H \quad (2)$$

or a concerted mechanism in which the methylation agent directly reacts with the alkene or arene.[1–13]

$$CH_3OR + C_nH_{2n} + Z–H \rightarrow C_nH_{2n+1} + ROH + Z–H \quad (3)$$

During methanol-to-olefin (MTO) processes, arenes are methylated to form one of thirteen C_6–C_{12} methylbenzene species which co-catalyze the formation of light alkenes.[14–18] We have previously studied these arene interconversion pathways using density functional theory (DFT) calculations combined with maximum rate analysis to analyze the predominant methylation agent (CH_3OH or CH_3OCH_3) and methylation pathway (concerted or sequential).[19] Our findings suggest that benzene is preferentially methylated via the sequential mechanism, consistent with previous kinetic studies, the rate of which is limited by surface methylation with a spectating benzene ring. The presence of this spectating benzene ring stabilizes the surface methylation transition state, demonstrating cooperativity between channels and intersections within MFI. Neither the sequential nor the concerted mechanism dominates in the step-wise conversion of benzene to hexamethylbenzene; however, step-wise methylation barriers remain between 75 and 137 kJ mol^{-1} at MTO conditions (623 K) suggesting that the formation of higher methylated arenes is not kinetically limited. It is likely that, once formed, these large arene species are diffusion-limited and therefore eventually cause catalyst deactivation.[20–25]

The transient interconversion pathways and myriad surface intermediates in MTO render kinetic studies alone incapable of elucidating mechanisms governing these reaction networks; this prompts the use of density functional theory (DFT) to investigate complicated intertwined chemical pathways. However, in systems involving hundreds to thousands of elementary steps, analyzing DFT-barriers is cumbersome—commonly overcome through microkinetic modeling or kinetic Monte Carlo (KMC) simulations. Critical species formed during MTO (such as aromatics) suffer from mass-transport limitations in zeolites and their diffusion rates and length scales affect rates, selectivities, and catalyst stabilities which microkinetic modeling fails to capture.[26–30] Here, we present a novel KMC package which models H-ZSM-5 crystals across experimentally relevant time and length scales to understand the role of transport during arene interconversion reactions (~100 reactions) previously investigated using periodic dispersion-corrected DFT methods.

2. Methods

2.1 Density Functional Theory Methods

DFT calculations were performed using the Vienna ab initio simulation package (VASP)[31–34] in a fully periodic MFI unit cell. The Perdew-Burke-Ernzerhof (PBE)[35–37] form of the generalized gradient approximation (GGA) was used to determine exchange and correlation energies and the DFT-D3 method with Becke and Johnson

damping accounted for dispersive interactions.[38–40] Planewaves were constructed using the projector augmented-wave (PAW)[41,42] potentials with an energy cutoff of 400 eV. The Brillouin zone was sampled at the Γ-point for all calculations.[43]

The MFI structure, originally obtained from the IZA database,[44] was annealed using AIMD calculations. The structure was heated from 200 K to 800 K over 3000 fs, held at 800 K for 3000 fs, then cooled over 15000 fs while the lattice parameters and orthorhombic shape were fixed. The wavefunction for each step was converged to within 10^{-4} eV and one atom was fixed to prevent bulk translation. The final structure obtained after annealing and optimizing is 23 kJ mol^{-1} more stable than the directly optimized IZA structure (Fig. S1, in the Supporting Information, SI). These calculations were done to ensure stability within the baseline framework and to prevent framework restructuring from altering calculated activation and reaction energies, as described in detail elsewhere.[45]

All calculations were performed at the T11 tetrahedral site (T-site) in MFI, which gives access to both the straight channel and the channel intersection where arenes prefer to populate. Reactant, product, and transition states were optimized until the maximum force on any atom was < 0.05 eV $Å^{-1}$. Wave functions were converged to within 10^{-6} eV and all forces were computed using a fast Fourier transform (FFT) grid with a cutoff twice the planewave cutoff. No atoms were constrained in any DFT optimization, pathway, or transition state calculations.

Minimum energy pathways were estimated using the nudged elastic band (NEB)[46,47] method. NEB calculations used 16 images and wavefunctions converged to 10^{-4} eV with an FFT grid 1.5 times the size of the plane-wave cutoff. The maximum force on each atom in all images were converged to < 0.5 eV $Å^{-1}$. Initial transition state structures obtained from NEBs are used as inputs for the Dimer method,[48] which optimizes a pair of structures to determine the local curvature of the potential energy surface until ultimately converging on a saddle point. Dimer calculations were converged so that maximum forces on any atom < 0.05 eV $Å^{-1}$.

All reactant, product, and transition were manually generated, optimized, then systematically reoriented based upon the state's interaction with the acid site, as previously described.[19,49] Each systematically reoriented structure was re-optimized, with the same parameters as the initial optimization, to identify the minimum energy state. The lowest energy state obtained from these reorientations is used in all further analysis. These reorientations serve to extensively seed the potential energy surface and more accurately determine the energy of each state, as compared to a single DFT calculation. There is no guarantee that the lowest energy state identified by these systematic reorientations will represent the global minimum, rather these reorientations serve to extensively seed the potential energy surface and more accurately determine the energy of each state, as compared to a single DFT calculation.

Frequencies were calculated for all reactant, product, and transition states using a fixed displacement method where the adsorbates (e.g., CH_3OH and benzene) and AlO_4H of the acid site are displaced while all other framework atoms are fixed. Low-frequency modes (< 60 cm^{-1}) were replaced with 60 cm^{-1}, similar to previous work,[50,51] because low frequencies are inaccurate and contribute significantly to vibrational entropy terms. These frequency calculations are used to determine temperature-corrected enthalpies and free energies according to harmonic oscillator approximations for vibrational partition functions and ideal gas treatments of rotational and translational partition functions for bulk gas species.

2.2 Kinetic Monte Carlo Simulations

Enthalpy and entropy barriers from DFT were used as inputs for kinetic Monte Carlo simulations to stochastically model reaction rates and coverages. The KMC simulations model the zeolite as a grid of identical, non-interacting acid sites each with its own void region—i.e., an MFI crystal with one acid site at every

intersection and only at the T-11 position. These intersectional sites can be occupied by (at most) one C_6–C_{12} arene and one oxygenate molecule (CH_3OH, CH_3OCH_3, H_2O) H-bound to the acid site, which can also be bare (H–Z), deprotonated (Z^-), or occupied by a surface methyl species (CH_3–Z). These channel intersections in MFI are separated by straight and sinusoidal channels which effectively isolate these Brønsted acid sites from one another, supporting the non-interacting site model used here. Previous DFT calculations were completed on a single T-site,[19] so an Al atom was only placed at one T-site type in this KMC model.

Single-site KMC simulations (1×1×1 grids) model only a single adsorption site on the MFI crystal site at the T-11 position. These models do not account for diffusion limitations and therefore can be directly compared to maximum rate analyses. Multi-site KMC simulations, however, do account for diffusion limitations in the MFI-crystal. Five different multi-site crystal models are analyzed in multi-site KMC simulations: slab-a, slab-b, slab-c, inverse, and normal. All crystal models contain both edge sites, representative of the external face of the crystal where adsorptions occur, and interior sites, accessed via diffusion. Adsorptions and desorptions from edge sites around all crystal types are treated as quasi-equilibrated reactions such that the site occupancies are governed by gas-phase pressures and thermodynamics. Interior sites, however, are only accessed by diffusion through straight and sinusoidal channels within MFI. Transport of arene molecules between intersectional sites was modeled using diffusion barriers calculated by DFT methods described in Section 2.1 and interpreted using transition state theory, an appropriate rate model for large-barrier processes such as these. Diffusion was modeled only with bare protons (H–Z) in the crystal; transport of arene molecules to sites with CH_3–Z, CH_3OH*, and CH_3OCH_3* species was not explicitly modeled with DFT, but estimated with KMC simulations. However, the energies, geometric arrangements, co-adsorbate interactions of arene species and small oxygenate molecules are explicitly modeled and calculated by DFT—not dictated by KMC. Transport of small oxygenate molecules (CH_3OH, CH_3OCH_3, H_2O) is assumed to be rapid compared to reaction rates, and thus their transport is not directly modeled (i.e., adsorption, desorption, and diffusion of these species occur with negligible barriers and are quasi-equilibrated processes). Slab-type crystals only permit adsorption of species on to a particular facet of the MFI crystal. For instance, slab-a models only permit adsorption and desorption to occur on the (1,0,0) facet of MFI crystal (Figure 1a). Similarly, adsorption and desorption only occur from the (0,1,0) facet of slab-b models (Figure 1a) and the (0,0,1) facet of slab-c models (Figure 1a). Once adsorption has occurred, the species then diffuse to internal sites via the sinusoidal channel (slab-a and slab-c) or the straight channel (slab-b). Similarly, once species are formed at the internal sites of slab-models they must diffuse to the respective edge site to desorb. The exposed surface of MFI of its coffin-shaped crystals (depicted in Figure 1a) is dominated by the (010) surface,[52,53] making the slab-b model the most representative of an MFI crystal. 'Normal' models assume adsorption and desorption occurs from edge sites (Figure 1b, simplified for a 2-D model of a 5×5 grid, denoted with E), and that diffusion via the straight or sinusoidal channel must occur to reach an interior site (Figure 1b, denoted with I). Reaction events can occur at both edge and interior sites; therefore, for the simplified 2-D crystal model in Figure 1b, species can react at 16 sites without diffusing (edge sites) and then diffuse via the straight or sinusoidal channels to the 9 interior sites to react. 'Inverse' models contain only a single adsorption site, regardless of their overall dimensions. This adsorption site is defined as the innermost intersection of the crystal (Figure 1b, simplified for a 2-D model of a 5×5 grid, denoted with E). Quasi-equilibrated adsorption and desorption of species can only occur to this single edge site. Similar to the 'normal' model, reactions can occur at this single edge site, but to access the remaining 24 reactive sites, species must diffuse via the straight or sinusoidal channels. This model is used to emphasize the effects of diffusion more so than the 'normal' crystal model because diffusion must occur for species to reach the majority of reactive sites.

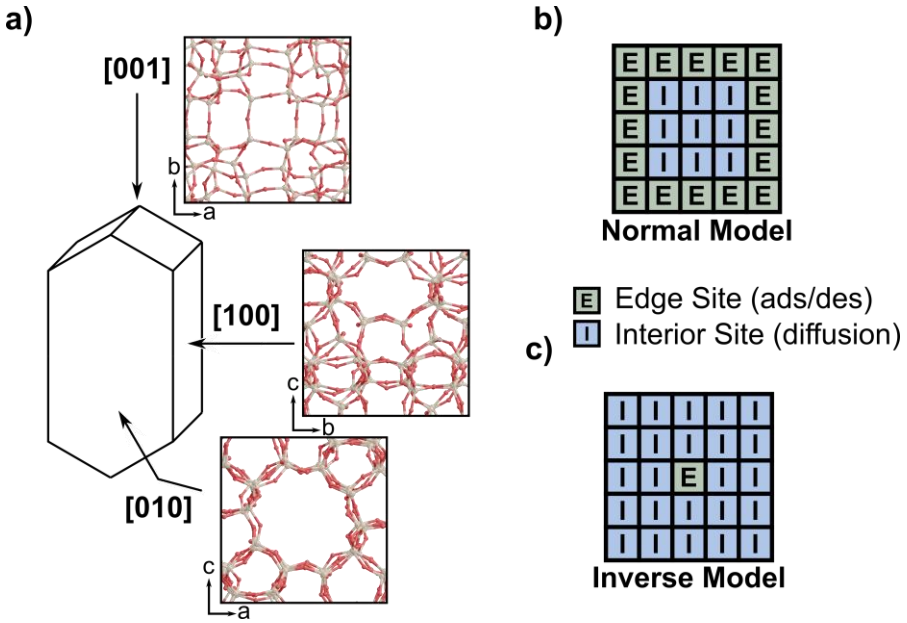

Figure 1. Representations of different KMC crystal models. a) Slab-models showing different facets of the coffin-shaped MFI crystal where slab-a represents the [100] facet, slab-b represents the [010] facet, and slab-c represents the [001] facet, b) simplified 2-D model of a 5×5 'normal' model with 16 edge sites (green, E) accessed by adsorption and 9 internal sites (blue, I) accessed by diffusion, and c) simplified 2-D model of a 5×5 'inverse' model with 1 edge site (green, E) located at the innermost site accessed via adsorption and 24 interior sites (blue, I) accessed via diffusion.

2.3 A Brief Description of the KMC Code

This KMC code is written in a combination of Python and Fortran. Input files include a list of adsorbed states along with their enthalpies and entropies; a list of gas-phase enthalpies and entropies; a list of reactions with activation and reaction enthalpies and entropies; a list of diffusions with enthalpy and entropy barriers along straight and sinusoidal axes for each diffusion-based molecule; and a file containing settings (crystal file and morphology) as well as conditions. Notably, adsorption enthalpies and entropies are not specified, these are automatically calculated based on the user-provided gas- and adsorbed-site enthalpies and entropies which greatly reduces the complexity of setting up these input files and reduces the potential for human error creating thermodynamically inconsistent input data. Python is used to interpret these user-friendly input files, enumerate the possible states of each site, chemical surface reactions, and the sites within the crystal. The Python code also creates a reaction map which identifies relevant reactions associated with each state and creates a site map which identifies site-numbers for neighboring sites along the sinusoidal and straight channel axis. The reaction map accelerates the later KMC routine because it eliminates the need to loop over all reactions to determine if they are possible given the state of a site. Similarly, the diffusion map eliminates the need to identify neighbors within the KMC routine. These diffusion and reaction maps are also formatted, along with state, site, and reaction enumerations, into Fortran-friendly output files (less user-friendly than the original input files). The Python code is typically run prior to runtime (i.e., as part of the setup workflow). The Fortran code does the actual KMC simulation iterating through event-time as consistent with other KMC routines.[54]

This KMC code uses temporal acceleration to throttle rapid quasi-equilibrated reactions such that more irreversible reactions occur within each simulation.[54] This is achieved monitoring the total number of reaction events (reverse + forward) compared to their net count (forward – reverse). When this value exceeds a desired

target, the forward and reverse rate is equally scaled to reduce the total frequency of the reaction (without effecting the net rate or the equilibrium constant). The occurrence of any irreversible step resets all scaling factors, allowing reaction networks to shift from one kinetic regime to another without bias. The aggressiveness of this temporal acceleration was varied by adjusting the desired total-over-net ratio (DTON) to ensure that it has no impact on overall reaction rates, but only on the number of catalytic turnovers observed within a KMC study.

3. Results and Discussion

3.1 Arene Diffusion

Diffusion of arene molecules is modeled as site-hopping from one T-11 intersection to an intersection with no acid site. Diffusion for all species was modeled through the straight and sinusoidal channels, with multiple orientations of the arene molecules. Diffusion down the straight channel was modeled in six different orientations for each species (Fig. 2, shown with hexamethylbenzene) varying in their orientation relative to the zeolite pore and varying the direction of arene moieties during diffusion—i.e., whether a methyl group (Fig. 2 a, c, e) or ring C–C bond (Fig. 2 b, d, f) 'led' the arene species through the straight channel. Diffusions down the sinusoidal channel were modeled with two orientations, where the species was 'led' by a methyl-substituent or a bond.

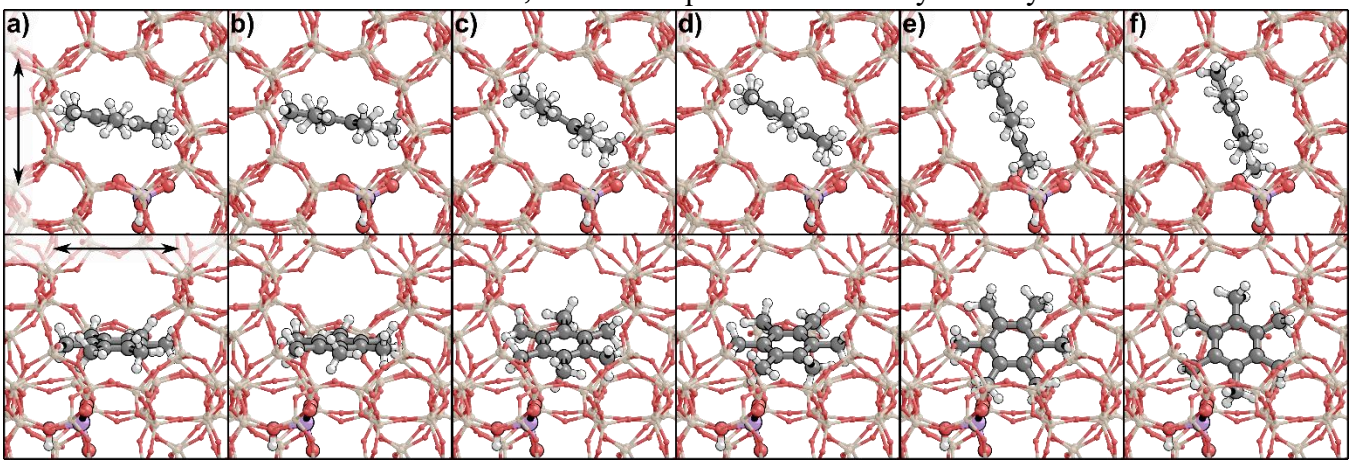

Figure 2. Tested orientations of arene species down the straight channel, shown with hexamethylbenzene. a) orientation 1 with a leading methyl group, b) orientation 1 with a leading bond, c) orientation 2 with a leading methyl group, d) orientation 2 with a leading bond, e) orientation 3 with a leading methyl group, and f) orientation 3 with a leading bond. Views are shown down the straight (top) and sinusoidal (bottom) channels. Arrows in a) represent the direction of diffusion in the pore.

Diffusion down the straight channel of MFI is always more facile than diffusion via the sinusoidal channel (Table 1). Diffusion barriers of benzene and toluene down the straight channel are < 40 kJ mol^{-1}, suggesting that this diffusion is relatively facile, while barriers of diffusion via the sinusoidal channel are 80–90 kJ mol^{-1}. *Para*-xylene diffusion barriers 20–30 kJ mol^{-1} lower than *ortho*- and *meta*-xylene, consistent with previous experimental results suggesting that *para*-xylene is the primary product of toluene methylation because of diffusive limitations,[29,55–57] though DFT calculations also indicate that *para*-xylene is also preferentially formed during methylation of toluene at MTH conditions.[19] 1,2,4-trimethylbenzene has significantly lower diffusion barriers than 1,2,3- and 1,3,5-tetramethylbenzene because the arrangement of methyl-substituents around 1,2,4-trimethylbenzene allows for minimal interaction with the surrounding framework among trimethylbenzene

species. Specifically, 1,2,3- and 1,3,5-trimethylbenzene have larger effective radii during diffusion than 1,2,4-trimethylbenznee, contributing to their higher diffusion barriers. Similarly, 1,2,4,5-tetramethylbenzene has a smaller effective radius than 1,2,3,4- and 1,2,3,5-tetramethylbenzene making diffusion of these species more facile. Generally, diffusion barriers tend to increase as the effective radii of the methylbenzene species increases, suggesting that higher methylated arenes (C_{10+}) will be diffusion limited compared to smaller species (C_6–C_9).

Table 1. DFT calculated barriers for diffusion down the straight and sinusoidal channels

	Straight Channel			**Sinusoidal Channel**		
	$\Delta G^{\ddagger}$	ΔH	ΔS	ΔG	ΔH	ΔS
Arene	*kJ mol*$^{-1}$	*kJ mol*$^{-1}$	*J mol*$^{-1}$ *K*$^{-1}$	*kJ mol*$^{-1}$	*kJ mol*$^{-1}$	*J mol*$^{-1}$ *K*$^{-1}$
Benzene	39	25	−37	50	40	−27
Toluene	34	26	−21	100	88	−32
Ortho-xylene	62	46	−43	121	109	−33
Meta-xylene	50	38	−31	88	81	−21
Para-xylene	30	23	−19	59	52	−19
1,2,3-triMB	110	94	−43	205	192	−33
1,2,4-triMB	47	47	0	146	146	0
1,3,5-triMB	181	107	−37	215	205	−27
1,2,3,4-tetraMB	115	94	−57	183	165	−47
1,2,3,5-tetraMB	152	123	−76	227	195	−53
1,2,4,5-tetraMB	50	53	−43	137	125	−33
pentaMB	169	150	−50	222	200	−60
hexaMB	194	175	−50	247	225	−60

Values reported are preliminary and at 373 K

3.2 Diffusion-free 1×1×1 KMC model and maximum rate analysis

A reaction list containing all 21 methylbenzene interconversion pathways (benzene to hexamethylbenzene) with CH_3OH and CH_3OCH_3 was modeled on all crystal types at benzene methylation conditions (373 K, 0.68 bar CH_3OCH_3, 0.02 bar C_6H_6, 0.1% aromatic conversion) and MTO conditions (623 K, 0.08 bar CH_3OCH_3, 0.04 bar C_6H_6, 10% conversion). Results from the 1×1×1 crystal model, which neglect diffusion, are compared to results from previously published maximum rate analysis.[19] Maximum rate analysis asserts, one at a time, that a step is rate-determining and that all preceding steps are quasi-equilibrated; rate coefficients are subsequently calculated using transition state theory. Further explanation of maximum rate analysis and rate equations are discussed in Section S1 of the supplemental information.

During KMC simulations, the rates of rapid quasi-equilibrated reactions are artificially decreased after a user-specified number, desired total over net (DTON), of net-occurrences to allow slower, rate-determining steps to occur. The rate of the reaction can be sensitive to this DTON value; therefore, a range of DTON values was tested

to determine a value of DTON to which rates in the 1×1×1 crystal model are no longer sensitive (Fig. 2). The rate of the 1×1×1 KMC simulations, determined by the net number of benzene adsorption events, is constant from DTON values of 50–1000 at both benzene methylation and MTO conditions. Therefore, DTON = 500 was used for all reactions described in this section.

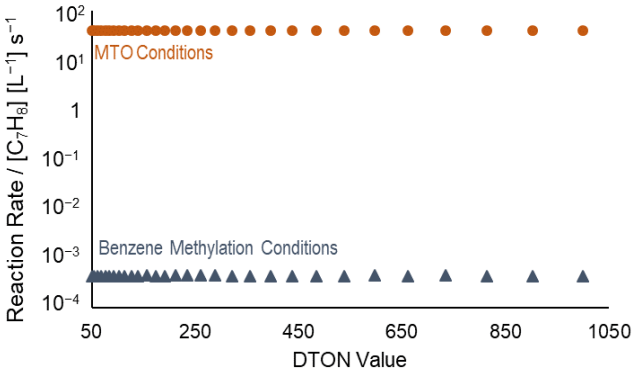

Figure 3. Net rates of benzene adsorption with varying DTON values at benzene methylation conditions (373 K, 0.68 bar CH_3OCH_3, 0.02 bar C_6H_6, 0.1% C_6H_6 conversion, triangles) and MTO conditions (623 K, 0.08 bar CH_3OCH_3, 0.02 bar C_6H_6, 10% C_6H_6 conversion, circles).

The rates obtained from maximum rate analysis and those obtained from the 1×1×1 crystal model KMC simulation are shown in Fig. 4. At benzene methylation conditions (373 K, 0.68 bar CH_3OCH_3, 0.02 bar C_6H_6, 0.1% aromatic conversion), the 1×1×1 KMC simulations predict that over 99% of the product is toluene. Both maximum rate analysis and KMC predict that benzene is methylated via the sequential mechanism and that at 373 K (benzene methylation temperatures) the rate is controlled by the formation of CH_3–Z species, which primarily occurs with a spectating benzene. Between 353–443 K, the rates predicted by maximum rate analysis and KMC agree well (Fig. 4a). However, above 443 K, the rate predicted by KMC is higher than that of maximum rate analysis. This deviation is caused by the assumption in maximum rate analysis that a single surface methylation mechanism dominates; in the KMC model, however, both surface methylation mechanisms (with and without a spectating arene species) contribute to the rate of CH_3–Z formation. For instance, maximum rate analysis predicts the rate of CH_3–Z formation with spectating benzene is 2×10^{-2} and in an empty pore the maximum rate is 1.9×10^{-2} at 463 K; therefore, the overall rate of CH_3–Z formation is predicted to be 2×10^{-2} as maximum rate analysis only considers the rate of the dominant CH_3–Z formation mechanism. However, KMC does not preclude one mechanism from occurring and therefore the rates of these two mechanisms are additive rather than controlled by solely the dominating step. Below 443 K, the rate of CH_3–Z formation with a spectating benzene is 10^2–10^3 times higher than that in an empty pore; therefore, the exclusion of CH_3–Z formation in an empty pore during maximum rate analysis does not contribute significantly to inaccurate predictions, compared to higher temperatures at which both mechanisms contribute to CH_3–Z formation.

Both maximum rate analysis and KMC suggest that rates are independent of CH_3OCH_3 pressure and a sub-linearly dependent on C_6H_6 pressure; previous kinetic studies investigating benzene methylation demonstrate a zero-order dependence on CH_3OCH_3 pressure and a linear dependence on C_6H_6 pressure (373 K, 0.68 bar CH_3OCH_3, 0.01–0.07 bar C_6H_6, 0.1% aromatic conversion).[12] This slight deviation from linearity in the maximum rate analysis and KMC models is likely caused by a slight over-prediction (~4 kJ mol^{-1}) in the binding energy of benzene.

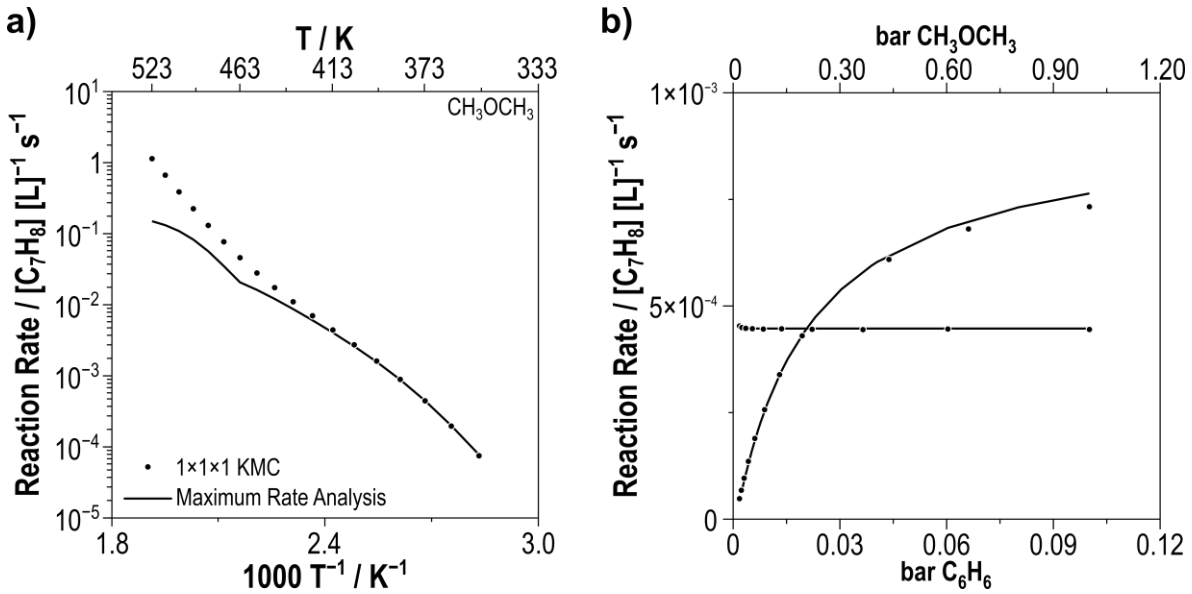

Figure 4. Overall rates of benzene methylation by CH_3OCH_3 as calculated by maximum rate analysis (line) and a single site (1×1×1) KMC calculation with varying a) temperature and b) CH_3OCH_3 and C_6H_6 pressure. Data are reported at 373 K, 0.2 bar C_6H_6, 0.68 bar CH_3OCH_3, and 0.1% aromatic conversion unless otherwise specified.

The same reaction list containing all 21 methylbenzene interconversion pathways was also analyzed using KMC at conditions typical of MTO processes (623 K, 0.08 bar CH_3OCH_3, 0.04 bar C_6H_6, 10% conversion). These KMC simulations predict that the product distribution switches from 99% toluene to also include di-, tri-, and tetramethylbenzene species at MTO conditions—confirming that the conditions at which KMC calculations are performed alter the product selectivity. KMC predicts the two predominant products are toluene and 1,3,5-trimethylbenzene, accounting for over 90% of the product distribution (Fig. 5). Methylbenzene is formed via sequential methylation of benzene and 1,3,5-tetramethylbenzene is formed from sequential methylation of *meta*-xylene, present from adsorption, (pressure of 4×10^{-4} bar, obtained from the assumption 10% of benzene is converted to toluene and 10% of toluene is converted into dimethylbenzenes), indicating that sequential methylation is the predominant mechanism of methylation for all arene species. This differs from previous predictions made by maximum rate-analysis because maximum-rate analysis 1) did not allow for adsorption of multiple species and 2) assumed that formation of CH_3–Z only occurred in the presence of a spectating ring—thus making it unfavorable compared to concerted methylation. Consideration of the adsorption of multiple species and incorporation of two CH_3–Z forming pathways was emitted from maximum rate-analysis to simplify the analysis. However, these limitations of using maximum rate analysis to analyze complex reaction networks with multiple possible rate-determining steps can be overcome with KMC.

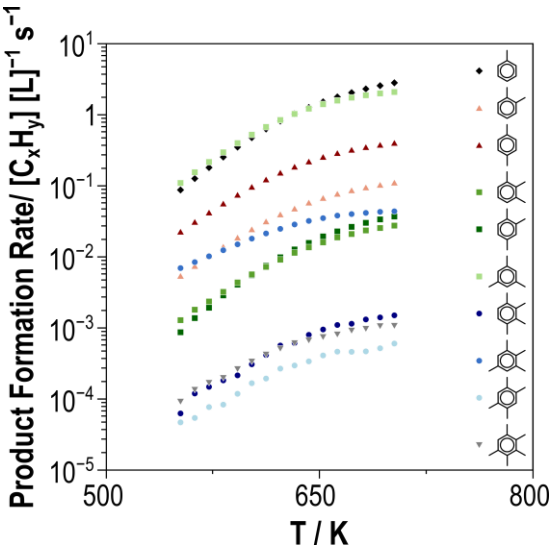

Figure 5. Net rate of arene desorption at MTO conditions (0.08 bar CH_3OCH_3, 0.04 bar C_6H_6, 10% conversion) varied from 523–703 K on a 1×1×1 crystal model.

The accuracy of the single-site, diffusion-free model is limited particularly in the formation of larger arene species. Highly substituted arene species that form at the interior of an MFI crystal are more likely to remain there because of mass transport limitations which are not captured in this 1×1×1 KMC model. Therefore, a similar analysis is performed on multi-site crystals, which incorporate diffusion limitations, for both the benzene methylation and MTO regimes.

Section 3.3 Normal and Inverse Crystals

We have evaluated the rates of all 21 interconversion pathways at benzene methylation conditions and at MTO conditions on multi-site crystals using both the 'normal' and 'inverse' models. Using these models, the effects of mass-transport limitations on the rate of reaction can be analyzed. We have evaluated 6 different crystal models: 3×3×3 'normal' and 5×5×5 'normal' and 'inverse' models. The total number of sites, number of edge sites, and number of internal sites are listed in Table 2. The maximum amount that the rate will decrease, relative to the maximum rate determined by a 1×1×1 crystal model, is proportional to the amount of edge sites (i.e., sites that do not require diffusion for a reaction to occur). For instance, a 1×1×1 crystal model represents the maximum reaction rate and contains 100% edge sites whereas only 78% of the sites are edge sites 5×5×5 normal model; indicating that rates drop by a maximum factor of ~12% in a 5×5×5 normal model if chemistry only occurs at edge sites, suggesting that the drop in rates for normal crystals will be a maximum of 60% in the 13×13×13 model (Table 2). Alternatively, in a 5×5×5 'inverse' crystal there is a single edge site and to reach the other 124 sites the species must diffuse either via the straight or sinusoidal channels. As such, the decrease in rate will be drastic compared to the 'normal' model, assuming species are mass transport-limited, as diffusion must occur to reach 99% of the sites.

Table 2. Total, edge, and internal sites for different crystal models.

Crystal	Total sites	Edge sites (%)		Internal sites (%)	
		Normal	Inverse	Normal	Inverse
3×3×3	27	96	4	4	96

5×5×5	125	78	1	12	99
7×3×3	63	29	–	71	–
3×7×3	63	29	–	71	–
3×3×7	63	29	–	71	–

DTON values were tested on the 3×3×3 ‘normal’ and ‘inverse’ multi-site models. Net rates of benzene adsorption remain consistent over the entire range for the 3×3×3 ‘normal’ model; therefore, a DTON = 500 was chosen for all calculations evaluating arene methylations on this model. However, in the 3×3×3 ‘inverse’ model the net rate of benzene adsorption becomes inconsistent at values of DTON > 300. The 3×3×3 ‘inverse’ model has a single edge site; therefore, diffusion to internal sites is necessary for a significant amount of reaction events to occur—as compared to the 3×3×3 ‘normal’ model in which reactions can occur at 96% of the sites without diffusing into an interior site. At high values of DTON, not enough reaction events are sampled to obtain a reliable rate of reaction, because the system spends the majority of iterations sampling adsorptive and diffusive events. Therefore, a value of DTON = 200 was selected for all calculations involving the 3×3×3 ‘inverse’ model.

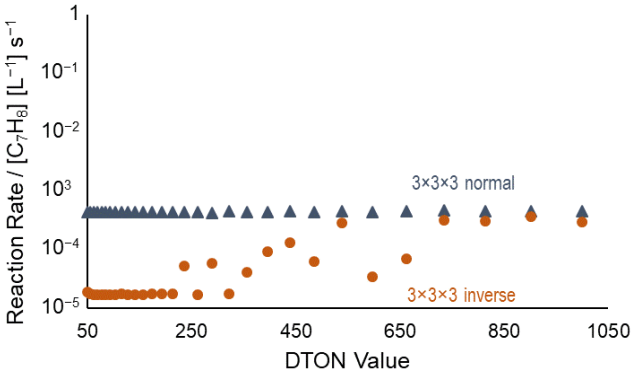

Figure 6. Net rate of benzene adsorption varied with DTON value for the 3×3×3 ‘normal’ (triangles) and ‘inverse’ (circles) models at benzene methylation conditions (373 K, 0.68 bar CH_3OCH_3, 0.02 bar C_6H_6, 0.1% aromatic conversion).

The rate of benzene methylation varied with CH_3OCH_3 pressure (373 K, 0.02 bar C_6H_6, 0.1% C_6H_6 conversion) was examined on 3×3×3 ‘normal’ model (Fig. 6). The 3×3×3 ‘normal’ model contains a total of 27 sites, 26 of which are edge sites and 1 of which is an internal site, indicating that diffusive restraints should not lower the rate by more than 4%. The rate of benzene methylation in the 3×3×3 ‘normal’ model is ~98% of the 1×1×1 model at all CH_3OCH_3 pressures (Fig. 5) which falls within the expected range based on the percent of internal and edge sites (Table 2). Similar to the 1×1×1 model, the 3×3×3 ‘normal’ model predicts over 99% of the product toluene. The primary diffusion modes for benzene and toluene to the interior site is via the straight channel, because diffusion via the straight channel is facile compared to the sinusoidal channel (Table 1). The species remaining on the edge and in the internal sites at the end of the simulation can be evaluated with this

KMC model, and the majority of species present on edge sites were CH_3OCH_3 and C_6H_6; however, seven of the ten KMC pressure runs had hexamethylbenzene present at the internal site causing deactivation of that site.

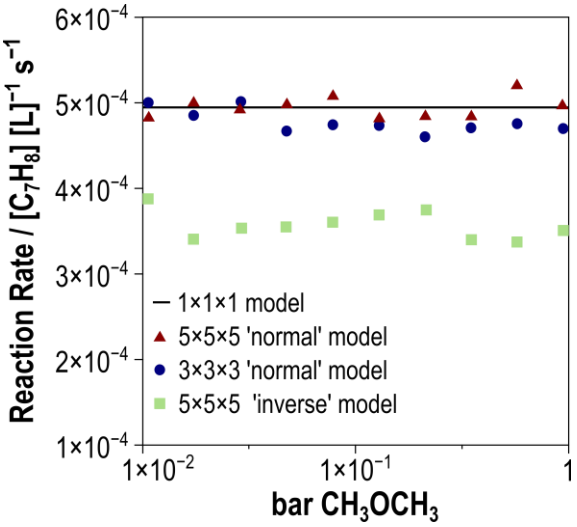

Figure 7. Rates of toluene formation at benzene methylation conditions (373 K, 0.02 bar C_6H_6, 0.1% C_6H_6 conversion) with varying (0.01–1 bar) pressure of CH_3OCH_3 pressure of the 1×1×1 (line), 3×3×3 'normal' (circle, blue), 5×5×5 'normal' (triangle, red), and 5×5×5 'inverse' (square, green) models.

Benzene methylation was also examined on 5×5×5 'normal' and 'inverse' models to compare the effects of diffusion. Both models contain a total of 125 sites; however, the normal model contains 78% edge sites (98) and 12% interior sites (27) while the inverse model contains 1% edge sites (1) and 99% interior sites (124)—thus making the effects of diffusion much more prominent in the 'inverse' model. Both models predict that the main product is toluene; however the diffusive limitations associated with adsorbing benzene species to internal sites is apparent in the 'inverse' model where rates are ~80% lower than the 1×1×1 model illustrating that as species grow in size, for example at MTO conditions, there will be a significant contribution to the rates because of mass-transport limitations.

Section 3.4 Slab Models

Three slab-models are used here: slab-a (7×3×3), slab-b (3×7×3), and slab-c (3×3×7) (Fig. 1a). Slab-models are used to isolate the effects of diffusion down the straight (slab-b) and sinusoidal channels (slab-a and slab-c). Each slab model contains a total of 63 sites and 7 edge sites located on the respective facet of the slab-model. For instance, in a slab-b model adsorption can occur onto the [010] facet.

The rate of benzene methylation, as defined by the net occurrences of benzene adsorption, was tested as a function of CH_3OCH_3 pressure. The rates of the three slab-models are nearly identical, suggesting that benzene and toluene are not diffusively limited down the straight or sinusoidal channels (Fig. 8a). On average, the rates of the slab-models are 80% lower than those of the 1×1×1 model, likely because of site deactivation caused by the presence of large, mass transport limited species. Similar to the 'normal' and 'inverse' models, the species remaining once the simulation has ended can be analyzed. Out of the 10 runs varying CH_3OCH_3 every run had between 5–21 sites containing hexamethylbenzene, corresponding to a maximum of 33% of sites deactivated within the system. Notably, the model that demonstrated the highest amounts of sites deactivated by hexamethylbenzene was slab-b—likely because more sites are accessible via diffusion.

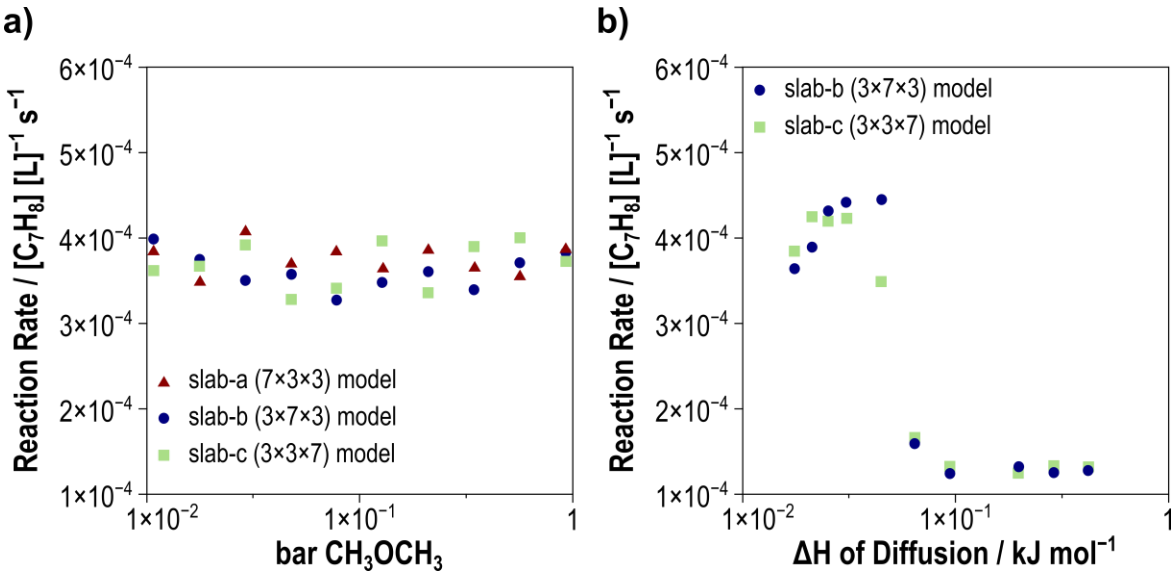

Figure 8. Net rate of toluene formation on a) slab-a, slab-b, and slab-c models at benzene methylation conditions (373 K, 0.02 bar C_6H_6, 0.1% C_6H_6 conversion) and varying CH_3OCH_3 pressures and b) slab-b and slab-c models artificially varying benzene adsorption enthalpies to determine the effects of mass-transport limitations on rates.

The effects of diffusion can be analyzed in each slab-model by artificially varying the barrier of benzene diffusion via the straight and sinusoidal channels. Straight and sinusoidal enthalpic diffusion barriers were varied from 20–200 kJ mol^{-1} in slab-b (3×7×3) and slab-c (3×3×7) models while artificially setting $\Delta H_{straight}=\Delta H_{sinusoidal}$ (Fig. 8b). There is drastic decrease in the rate between diffusion barriers of 80 and 100 kJ mol^{-1} caused by diffusive limitations. This suggests that species with diffusional barriers larger than 80 kJ mol^{-1}, such as penta- and hexamethylbenzene, will be significantly limited in mass-transport during multi-site kinetic models.

4. Conclusions

A list containing C_6–C_{12} methylbenzene sequential and concerted interconversion pathways with CH_3OH CH_3OCH_3 (~100 elementary steps) was analyzed with a novel KMC package that models H-ZSM-5 crystals across experimentally relevant time and length scales to understand the integrated roles of transport and kinetics.

Transport of arene species was modeled with DFT via site hopping from one T11 intersection to a T-site with no acid-site via either the straight or sinusoidal channels. Each diffusion was modeled in different orientations, based on the orientation of the methylbenzene relative to the pore and varying the direction of arene moieties during diffusion—i.e., whether a methyl group or ring C–C bond 'led' the arene species through the channels. The diffusion barrier associated with each species trends will the effective radius—those species that have a small effective radius such as benzene, toluene, *para*-xylene, 1,2,4-trimethylbenzene, and 1,2,4,5-tetramethylbenzene are not as diffusion limited as their larger radii methylbenzene isomers.

The results of a single site KMC simulation, neglecting diffusive limitations, are compared to previously reported maximum rate analyses of arene interconversion pathways at benzene methylation conditions (373 K, 0.68 bar CH_3OCH_3, 0.02 bar C_6H_6, 0.1% C_6H_6 conversion) and conditions more representative of MTO (623 K, 0.08 bar CH_3OCH_3, 0.04 bar C_6H_6, 10% conversion). At benzene methylation conditions, KMC predicts that over 99% of the product is toluene, consistent with expectations. KMC and maximum rate analysis demonstrate good

agreement regarding rate dependencies on temperature and pressure at benzene methylation conditions—demonstrating the reliability of these KMC simulations. We demonstrate that at MTO conditions the product distribution changes to include di- and tri-tetramethylbenzenes species as well as toluene (in contrast to AM conditions). Here, we demonstrate that the limitations of maximum rate analysis with analyzing complex reaction networks with multiple possible rate-determining steps and a large complex set of potential abundant surface intermediates can be overcome with KMC.

Arene methylation interconversion at benzene methylation conditions were also analyzed with 'normal, 'inverse', and slab-type models that incorporate diffusive limitations. In these larger models, it is not uncommon for large species, such as hexamethylbenzene to form and become 'trapped' at interior sites thus causing site deactivation. Generally, 10–20% of sites in a model will become deactivated because of mass-transport limitations—demonstrating the importance of incorporating diffusive limitations into analysis of reaction pathways occurring within zeolite catalysts. Additionally, to further evaluate the effects of diffusive limitations—diffusion barriers were artificially varied from 20–200 and rates drastically decrease between diffusion barriers of 80 and 100 kJ mol^{-1} –suggesting that species with diffusional barriers larger than 80 kJ mol^{-1}, such as penta- and hexamethylbenzene, will be significantly limited in mass-transport during multi-site kinetic models for benzene methylation. Overall, this study serves as a proof-of-concept for a novel KMC package that expedites rate analysis of complex reaction pathways and introduces mass-transport limitations which are not commonly accounted for in analysis of theoretical results. This novel KMC package can predict the behavior of diffusion-limited species, such as penta- and hexamethylbenzene, and the mechanisms through which they are formed and eventually lead to catalyst deactivation.

Bibliography

(1) Ghorbanpour, A.; Rimer, J. D.; Grabow, L. C. Computational Assessment of the Dominant Factors Governing the Mechanism of Methanol Dehydration over H-ZSM-5 with Heterogeneous Aluminum Distribution. *ACS Catal.* **2016**, *6*, 2287–2298 DOI: 10.1021/acscatal.5b02367.

(2) Jones, A. J.; Iglesia, E. Kinetic, spectroscopic, and theoretical assessment of associative and dissociative methanol dehydration routes in zeolites. *Angew. Chem. Int. Ed. Engl.* **2014**, *53*, 12177–12181 DOI: 10.1002/anie.201406823.

(3) Van Speybroeck, V.; Van der Mynsbrugge, J.; Vandichel, M.; Hemelsoet, K.; Lesthaeghe, D.; Ghysels, A.; Marin, G. B.; Waroquier, M. First principle kinetic studies of zeolite-catalyzed methylation reactions. *J. Am. Chem. Soc.* **2011**, *133*, 888–899 DOI: 10.1021/ja1073992.

(4) Svelle, S.; Kolboe, S.; Swang, O.; Olsbye, U. Methylation of alkenes and methylbenzenes by dimethyl ether or methanol on acidic zeolites. *J. Phys. Chem. B* **2005**, *109*, 12874–12878 DOI: 10.1021/jp051125z.

(5) Wen, Z.; Yang, D.; He, X.; Li, Y.; Zhu, X. Methylation of benzene with methanol over HZSM-11 and HZSM-5: A density functional theory study. *J. Mol. Catal. A: Chem* **2016**, *424*, 351–357 DOI: 10.1016/j.molcata.2016.07.051.

(6) Hill, I. M.; Hashimi, S. A.; Bhan, A. Kinetics and mechanism of olefin methylation reactions on zeolites. *J. Catal.* **2012**, *285*, 115–123 DOI: 10.1016/j.jcat.2011.09.018.

(7) Svelle, S.; Kolboe, S.; Olsbye, U.; Swang, O. A Theoretical Investigation of the Methylation of Methylbenzenes and Alkenes by Halomethanes over Acidic Zeolites. *J. Phys. Chem. B* **2003**, *107*, 5251–5260 DOI: 10.1021/jp030101u.

(8) Arstad, B.; Kolboe, S.; Swang, O. A theoretical investigation on the methylation of methylbenzenes on zeolites. *J. Phys. Chem. B* **2002**, *106*, 12722–12726 DOI: 10.1021/jp020851o.

(9) Svelle, S.; Rønning, P. O.; Kolboe, S. Kinetic studies of zeolite-catalyzed methylation reactions1. Coreaction of [12C]ethene and [13C]methanol. *J. Catal.* **2004**, *224*, 115–123 DOI: 10.1016/j.jcat.2004.02.022.

(10) Svelle, S.; Arstad, B.; Kolboe, S.; Swang, O. A Theoretical Investigation of the Methylation of Alkenes with Methanol over Acidic Zeolites. *J. Phys. Chem. B* **2003**, *107*, 9281–9289 DOI: 10.1021/jp022201q.

(11) Svelle, S.; Visur, M.; Olsbye, U.; Saepurahman; Bjørgen, M. Mechanistic Aspects of the Zeolite Catalyzed Methylation of Alkenes and Aromatics with Methanol: A Review. *Top. Catal.* **2011**, *54*, 897–906 DOI: 10.1007/s11244-011-9697-7.

(12) Hill, I.; Malek, A.; Bhan, A. Kinetics and Mechanism of Benzene, Toluene, and Xylene Methylation over H-MFI. *ACS Catal.* **2013**, *3*, 1992–2001 DOI: 10.1021/cs400377b.

(13) De Wispelaere, K.; Martínez-Espín, J. S.; Hoffmann, M. J.; Svelle, S.; Olsbye, U.; Bligaard, T. Understanding zeolite-catalyzed benzene methylation reactions by methanol and dimethyl ether at operating conditions from first principle microkinetic modeling and experiments. *Catal. Today* **2018**, *312*, 35–43 DOI: 10.1016/j.cattod.2018.02.042.

(14) Lesthaeghe, D.; Horré, A.; Waroquier, M.; Marin, G. B.; Van Speybroeck, V. Theoretical insights on methylbenzene side-chain growth in ZSM-5 zeolites for methanol-to-olefin conversion. *Chem. Eur. J* **2009**, *15*, 10803–10808 DOI: 10.1002/chem.200901723.

(15) Ilias, S.; Bhan, A. The mechanism of aromatic dealkylation in methanol-to-hydrocarbons conversion on H-ZSM-5: What are the aromatic precursors to light olefins? *J. Catal.* **2014**, *311*, 6–16 DOI: 10.1016/j.jcat.2013.11.003.

(16) Wang, C.-M.; Wang, Y.-D.; Liu, H.-X.; Yang, G.; Du, Y.-J.; Xie, Z.-K. Aromatic-based hydrocarbon pool mechanism for methanol-to-olefins conversion in H-SAPO-18: A van der Waals density functional study. *Chinese Journal of Catalysis* **2015**, *36*, 1573–1579 DOI: 10.1016/S1872-2067(15)60891-9.

(17) Ilias, S.; Bhan, A. Tuning the selectivity of methanol-to-hydrocarbons conversion on H-ZSM-5 by co-processing olefin or aromatic compounds. *J. Catal.* **2012**, *290*, 186–192 DOI: 10.1016/j.jcat.2012.03.016.

(18) Mole, T. Aromatic co-catalysis of methanol conversion over zeolite catalysts. *J. Catal.* **1983**, *82*, 261–266 DOI: 10.1016/0021-9517(83)90192-6.

(19) DeLuca, M.; Kravchenko, P.; Hoffman, A.; Hibbitts, D. D. Mechanism and Kinetics of Methylating C6–C12 Methylbenzenes with Methanol and DME in H-MFI Zeolites. *ACS Catal. In Review, available as a pre-print on https://doi.org/10.26434/chemrxiv.8016017.v1*.

(20) Dai, W.; Wu, G.; Li, L.; Guan, N.; Hunger, M. Mechanisms of the Deactivation of SAPO-34 Materials with Different Crystal Sizes Applied as MTO Catalysts. *ACS Catal.* **2013**, *3*, 588–596 DOI: 10.1021/cs400007v.

(21) Seo, G.; Kim, J.-H.; Jang, H.-G. Methanol-to-Olefin Conversion over Zeolite Catalysts: Active Intermediates and Deactivation. *Catal. Surv. Asia* **2013**, *17*, 103–118 DOI: 10.1007/s10563-013-9157-4.

(22) Bjørgen, M.; Akyalcin, S.; Olsbye, U.; Benard, S.; Kolboe, S.; Svelle, S. Methanol to hydrocarbons over large cavity zeolites: Toward a unified description of catalyst deactivation and the reaction mechanism. *J. Catal.* **2010**, *275*, 170–180 DOI: 10.1016/j.jcat.2010.08.001.

(23) Olsbye, U.; Svelle, S.; Lillerud, K. P.; Wei, Z. H.; Chen, Y. Y.; Li, J. F.; Wang, J. G.; Fan, W. B. The formation and degradation of active species during methanol conversion over protonated zeotype catalysts. *Chem. Soc. Rev.* **2015**, *44*, 7155–7176 DOI: 10.1039/c5cs00304k.

(24) Hemelsoet, K.; Nollet, A.; Van Speybroeck, V.; Waroquier, M. Theoretical simulations elucidate the role of naphthalenic species during methanol conversion within H-SAPO-34. *Chem. Eur. J* **2011**, *17*, 9083–9093 DOI: 10.1002/chem.201100920.

(25) Rojo-Gama, D.; Nielsen, M.; Wragg, D. S.; Dyballa, M.; Holzinger, J.; Falsig, H.; Lundegaard, L. F.; Beato, P.; Brogaard, R. Y.; Lillerud, K. P.; et al. A Straightforward Descriptor for the Deactivation of Zeolite Catalyst H-ZSM-5. *ACS Catal.* **2017**, *7*, 8235–8246 DOI: 10.1021/acscatal.7b02193.

(26) Khare, R.; Bhan, A. Mechanistic studies of methanol-to-hydrocarbons conversion on diffusion-free MFI samples. *J. Catal.* **2015**, *329*, 218–228 DOI: 10.1016/j.jcat.2015.05.012.

(27) Losch, P.; Pinar, A. B.; Willinger, M. G.; Soukup, K.; Chavan, S.; Vincent, B.; Pale, P.; Louis, B. H-ZSM-5 zeolite model crystals: Structure-diffusion-activity relationship in methanol-to-olefins catalysis. *J. Catal.* **2017**, *345*, 11–23 DOI: 10.1016/j.jcat.2016.11.005.

(28) Bhan, A.; Tsapatsis, M. Zeolites with nanometer diffusion lengths and implications in shape selective catalysis. *Curr. Opin. Chem. Eng.* **2013**, *2*, 320–324 DOI: 10.1016/j.coche.2013.06.001.

(29) Gobin, O. C.; Reitmeier, S. J.; Jentys, A.; Lercher, J. A. Diffusion pathways of benzene, toluene and p-xylene in MFI. *Micropor. Mesopor. Mat.* **2009**, *125*, 3–10 DOI: 10.1016/j.micromeso.2009.01.025.

(30) Smit, B.; Maesen, T. L. M. Molecular simulations of zeolites: adsorption, diffusion, and shape selectivity. *Chem. Rev.* **2008**, *108*, 4125–4184 DOI: 10.1021/cr8002642.

(31) Kresse, G.; Hafner, J. *Ab initio* molecular dynamics for liquid metals. *Phys. Rev. B* **1993**, *47*, 558–561 DOI: 10.1103/PhysRevB.47.558.

(32) Kresse, G.; Hafner, J. Ab initio molecular-dynamics simulation of the liquid-metal-amorphous-semiconductor transition in germanium. *Phys. Rev. B, Condens. Matter* **1994**, *49*, 14251–14269 DOI: 10.1103/PhysRevB.49.14251.

(33) Kresse, G.; Furthmüller, J. Efficient iterative schemes for ab initio total-energy calculations using a plane-wave basis set. *Phys. Rev. B, Condens. Matter* **1996**, *54*, 11169–11186.

(34) Kresse, G.; Furthmüller, J. Efficiency of ab-initio total energy calculations for metals and semiconductors using a plane-wave basis set. *Comp. Mater. Sci.* **1996**, *6*, 15–50 DOI: 10.1016/0927-0256(96)00008-0.

(35) Perdew, J. P.; Burke, K.; Ernzerhof, M. Generalized gradient approximation made simple. *Phys. Rev. Lett.* **1996**, *77*, 3865–3868 DOI: 10.1103/PhysRevLett.77.3865.

(36) Zhang, Y.; Yang, W. Comment on "Generalized Gradient Approximation Made Simple. *Phys. Rev. Lett.* **1998**, *80*, 890–890 DOI: 10.1103/PhysRevLett.80.890.

(37) Hammer, B.; Hansen, L. B.; Nørskov, J. K. Improved adsorption energetics within density-functional theory using revised Perdew-Burke-Ernzerhof functionals. *Phys. Rev. B* **1999**, *59*, 7413–7421 DOI: 10.1103/PhysRevB.59.7413.

(38) Grimme, S.; Ehrlich, S.; Goerigk, L. Effect of the damping function in dispersion corrected density functional theory. *J. Comput. Chem.* **2011**, *32*, 1456–1465 DOI: 10.1002/jcc.21759.

(39) Schröder, H.; Creon, A.; Schwabe, T. Reformulation of the D3(Becke-Johnson) Dispersion Correction without Resorting to Higher than C_6 Dispersion Coefficients. *J. Chem. Theory Comput.* **2015**, *11*, 3163–3170 DOI: 10.1021/acs.jctc.5b00400.

(40) Grimme, S.; Antony, J.; Ehrlich, S.; Krieg, H. A consistent and accurate ab initio parametrization of density functional dispersion correction (DFT-D) for the 94 elements H-Pu. *J. Chem. Phys.* **2010**, *132*, 154104 DOI: 10.1063/1.3382344.

(41) Blöchl, P. E. Projector augmented-wave method. *Phys. Rev. B, Condens. Matter* **1994**, *50*, 17953–17979.

(42) Kresse, G.; Joubert, D. From ultrasoft pseudopotentials to the projector augmented-wave method. *Phys. Rev. B* **1999**, *59*, 1758–1775 DOI: 10.1103/PhysRevB.59.1758.

(43) Monkhorst, H. J.; Pack, J. D. Special points for Brillouin-zone integrations. *Phys. Rev. B* **1976**, *13*, 5188–5192 DOI: 10.1103/PhysRevB.13.5188.

(44) Baerlocher, C.; McCusker, L. B. Database of Zeolite Structures: http://www.iza-structure.org/databases. **2013**.

(45) Hoffman, A.; DeLuca, M.; David Hibbitts. Restructuring of MFI Framework Zeolite Models and their Associated Artifacts in DFT Calculations.

(46) Jónsson, H.; Mills, G.; Jacobsen, K. W. Nudged elastic band method for finding minimum energy paths of transitions. In *Classical and Quantum Dynamics in Condensed Phase Simulations*; Berne, B. J.; Ciccotti, G.; Coker, D. F., Eds.; World Scientific, 1998; pp. 385–404.

(47) Henkelman, G.; Jónsson, H. Improved tangent estimate in the nudged elastic band method for finding minimum energy paths and saddle points. *J. Chem. Phys.* **2000**, *113*, 9978–9985 DOI: 10.1063/1.1323224.

(48) Henkelman, G.; Jónsson, H. A dimer method for finding saddle points on high dimensional potential surfaces using only first derivatives. *J. Chem. Phys.* **1999**, *111*, 7010–7022 DOI: 10.1063/1.480097.

(49) Nystrom, S.; Hoffman, A.; Hibbitts, D. Tuning Brønsted acid strength by altering site proximity in CHA framework zeolites. *ACS Catal.* **2018**, *8*, 7842–7860 DOI: 10.1021/acscatal.8b02049.

(50) Herrmann, S.; Iglesia, E. Elementary steps in acetone condensation reactions catalyzed by aluminosilicates with diverse void structures. *J. Catal.* **2017**, *346*, 134–153 DOI: 10.1016/j.jcat.2016.12.011.

(51) Zhi, Y.; Shi, H.; Mu, L.; Liu, Y.; Mei, D.; Camaioni, D. M.; Lercher, J. A. Dehydration Pathways of 1-Propanol on HZSM-5 in the Presence and Absence of Water. *J. Am. Chem. Soc.* **2015**, *137*, 15781–15794 DOI: 10.1021/jacs.5b09107.

(52) Díaz, I.; Kokkoli, E.; Terasaki, O.; Tsapatsis, M. Surface structure of zeolite (MFI) crystals. *Chem. Mater.* **2004**, *16*, 5226–5232 DOI: 10.1021/cm0488534.

(53) de A. A. Soler-Illia, G. J.; Sanchez, C.; Lebeau, B.; Patarin, J. Chemical strategies of design textured materials: from microporous and mesoporous oxides to nanonetworks and hierarchichal structures. *ChemInform* **2003**, *34* DOI: 10.1002/chin.200303279.

(54) Dybeck, E. C.; Plaisance, C. P.; Neurock, M. Generalized temporal acceleration scheme for kinetic monte carlo simulations of surface catalytic processes by scaling the rates of fast reactions. *J. Chem. Theory Comput.* **2017**, *13*, 1525–1538 DOI: 10.1021/acs.jctc.6b00859.

(55) Pope, C. G. Sorption of benzene, toluene and p-xylene on ZSM-5. *J. Phys. Chem.* **1984**, *88*, 6312–6313 DOI: 10.1021/j150669a051.

(56) Kaeding, W. Selective alkylation of toluene with methanol to produce para-Xylene. *J. Catal.* **1981**, *67*, 159–174 DOI: 10.1016/0021-9517(81)90269-4.

(57) Kaeding, W. Shape-selective reactions with zeolite catalysts II. Selective disproportionation of toluene to produce benzene and p-Xylene. *J. Catal.* **1981**, *69*, 392–398 DOI: 10.1016/0021-9517(81)90174-3.